Development of a model of the coronary arterial tree for the 4D XCAT phantom

To cite this article: George S K Fung *et al* 2011 *Phys. Med. Biol.* **56** 5651

View the article online for updates and enhancements.

Development of a model of the coronary arterial tree for the 4D XCAT phantom

George S K Fung[1], **W Paul Segars**[2], **Grant T Gullberg**[3] **and Benjamin M W Tsui**[1]

[1] Department of Radiology, Johns Hopkins University, Baltimore, MD, USA
[2] Department of Radiology, Duke University, Durham, NC, USA
[3] E O Lawrence Berkeley National Laboratory, Life Science Division, Berkeley, CA, USA

E-mail: gfung2@jhmi.edu

Abstract

A detailed three-dimensional (3D) model of the coronary artery tree with cardiac motion has great potential for applications in a wide variety of medical imaging research areas. In this work, we first developed a computer-generated 3D model of the coronary arterial tree for the heart in the extended cardiac-torso (XCAT) phantom, thereby creating a realistic computer model of the human anatomy. The coronary arterial tree model was based on two datasets: (1) a gated cardiac dual-source computed tomography (CT) angiographic dataset obtained from a normal human subject and (2) statistical morphometric data of porcine hearts. The initial proximal segments of the vasculature and the anatomical details of the boundaries of the ventricles were defined by segmenting the CT data. An iterative rule-based generation method was developed and applied to extend the coronary arterial tree beyond the initial proximal segments. The algorithm was governed by three factors: (1) statistical morphometric measurements of the connectivity, lengths and diameters of the arterial segments; (2) avoidance forces from other vessel segments and the boundaries of the myocardium, and (3) optimality principles which minimize the drag force at the bifurcations of the generated tree. Using this algorithm, the 3D computational model of the largest six orders of the coronary arterial tree was generated, which spread across the myocardium of the left and right ventricles. The 3D coronary arterial tree model was then extended to 4D to simulate different cardiac phases by deforming the original 3D model according to the motion vector map of the 4D cardiac model of the XCAT phantom at the corresponding phases. As a result, a detailed and realistic 4D model of the coronary arterial tree was developed for the XCAT phantom by imposing constraints of anatomical and physiological characteristics of the coronary vasculature. This new 4D coronary artery tree model provides a unique simulation tool that can be used in the development and evaluation of

instrumentation and methods for imaging normal and pathological hearts with myocardial perfusion defects.

(Some figures in this article are in colour only in the electronic version)

1. Introduction

The four-dimensional (4D) extended cardiac-torso (XCAT) phantom (3D phantom with motion) is an extension of the NURBS-based cardiac-torso (NCAT) phantom (Segars 2001, Segars *et al* 2003, 2010, Segars and Tsui 2009), which has been widely used in medical imaging research to evaluate and improve 4D cardiac imaging techniques (McGurk *et al* 2010, Minarik *et al* 2009, Segars *et al* 2008, 2009a, Tang *et al* 2009). The XCAT phantom provides a realistic and flexible computer-generated model of the human anatomy and physiology based on the 'Visible Human' anatomical imaging data from the National Library of Medicine (Ackerman 1999). The 4D XCAT phantom also models cardiac and respiratory patient motions based on 4D tagged MRI data and 4D respiratory-gated CT data (Segars 2001, Segars *et al* 2010).

In clinical medical imaging, it is important to estimate a patient's potential risk for heart attack by imaging the coronary arteries to assess for stenoses and myocardial perfusion defects (MPDs). To achieve that, single photon emission computed tomography (SPECT) and positron emission tomography (PET) detect MPD by directly imaging the myocardial perfusion distribution by utilizing appropriate radiotracers. In CT, C-arm and magnetic resonance (MR) angiography, stenoses in coronary arteries are detected by utilizing appropriate contrast agents. To accurately evaluate these imaging methods, it is desirable to have a phantom that has a realistic and detailed coronary arterial tree, and presence of stenoses and MPDs, as they are found in representative clinical cases. At present, there is no realistic and detailed coronary arterial tree phantom available for medical imaging research. For instance, the current XCAT phantom is only capable of modeling the regional MPD as a pie-shaped wedge, which is likely not clinically realistic and its location is not related to any coronary arterial tree or stenosis.

In the 3D version of the XCAT phantom, i.e. the 4D XCAT phantom without the cardiac and respiratory patient motions, high-resolution dual-source CT coronary angiographic image data of a contrast-enhanced normal human heart was used to define the anatomical details of the cardiac layers and the initial segments of the coronary arterial tree (Segars *et al* 2007). However, even with this state-of-the-art imaging technique, only the largest two or three generations of the coronary arterial tree of the beating heart could be delineated. Further enhancements are required in order to incorporate a more realistic and more detailed model of the coronary arterial tree.

In this work, an iterative rule-based generation method (Garrity *et al* 2003, Kitaoka *et al* 1997) that systematically utilized anatomic, morphometric and physiologic principles was used to generate a more complete model of the coronary arterial tree for the 4D XCAT phantom. A number of computer algorithms that can be utilized to generate the coronary arterial tree of animal hearts have been proposed (Beard and Bassingthwaighte 2000, Kaimovitz *et al* 2005, Kaimovitz *et al* 2010, Smith *et al* 2000). However, they were all subject to a number of limitations: (1) the anatomy of the myocardium was based on canine hearts, or was defined by simplified geometrical shapes, such as a cylinder or a spheroid; (2) the initial coronary arterial trees were based on canine hearts, or were arbitrarily defined; (3) the morphometric data of the coronary arterial tree of a porcine heart were used directly without appropriate scaling, and (4) complicated and computationally intensive optimization methods were employed to
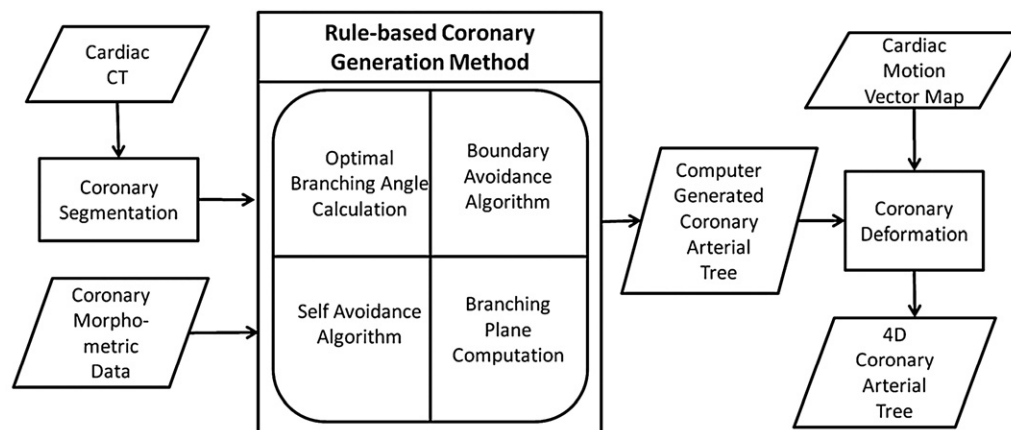
Figure 1. Flow chart of the overall detailed coronary arterial tree generation methods.

implement the tree generation algorithms. The advantages of our proposed method include: (1) the anatomic details of the myocardial surfaces and the initial coronary arterial tree were extracted from a set of state-of-the-art cardiac CT images of a normal human subject; (2) the statistical morphometric data of the coronary arterial tree of an average human subject were appropriately scaled from the original porcine heart data, and (3) a more flexible and faster rule-based iterative generation algorithm, used in our previous airway tree generation research (Garrity *et al* 2003, Kitaoka *et al* 1997), was adopted and modified for the coronary arterial tree generation. One of the potential applications of the detailed computer-generated coronary arterial tree is for the simulation of the realistic MPDs (Fung *et al* 2009) for medical imaging research based on the spatial distribution of the coronary arterial tree and the locations of the stenoses in it.

2. Methods

2.1. Overview

Figure 1 displays a flow chart detailing our methods used to generate the coronary arterial tree model for the 4D XCAT phantom. The anatomical data of the coronary arterial tree and the heart were segmented from a set of state-of-the-art cardiac CT images of a normal human subject, and the morphometric data of the coronary arterial tree were acquired from physiology literature (Kassab *et al* 1993, 1994, 1997, Kassab and Fung 1994). The rule-based coronary generation method was developed to extend the coronary arteries from proximal large branches to distal small branches distributed evenly over the myocardium. By deforming the generated 3D coronary arterial tree according to the motion vector map of the 4D XCAT phantom (Segars *et al* 2009b), the coronary arterial tree model was extended to 4D to model different phases of the beating heart.

2.1.1. Segmentation of the coronary arterial tree and heart wall layers. Defining the anatomical details of the coronary arterial tree and the heart wall was essential for generating an anatomically realistic model. A set of high spatial and temporal resolution dual-source cardiac-gated CT images of a normal human subject (provided by Siemens Healthcare) was
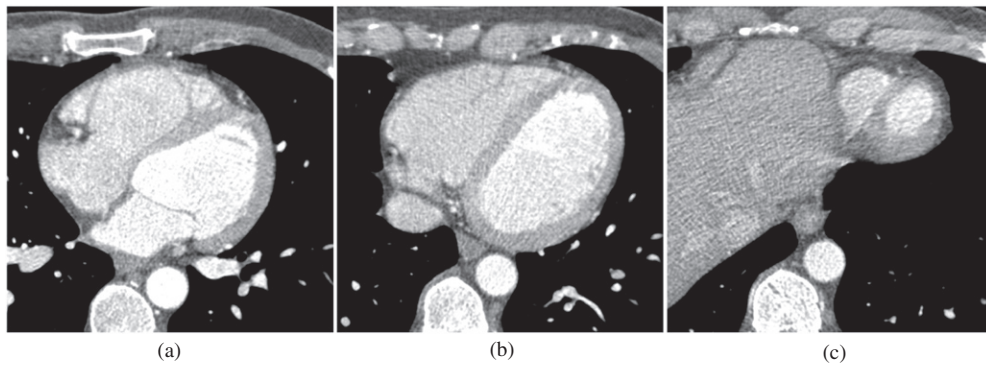
Figure 2. Sample transaxial cardiac CT images at the (a) superior, (b) mid and (c) inferior positions of a human heart and the coronary arteries at end-diastole.
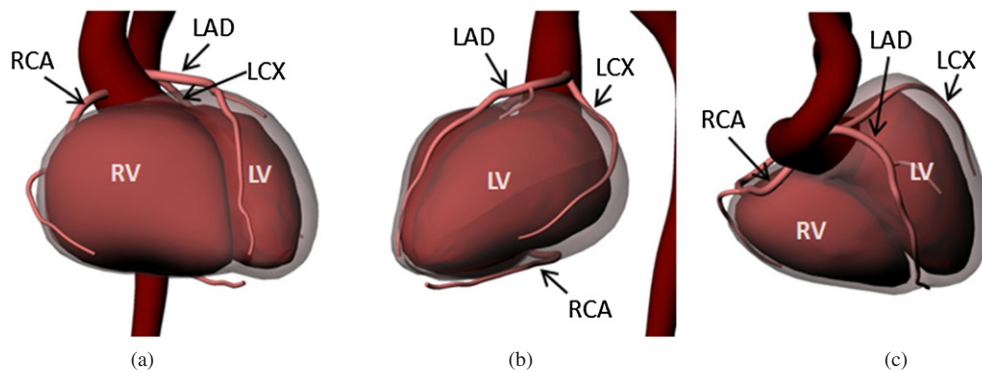
Figure 3. (a) Front, (b) left and (c) top views of the segmented major coronary arteries (LAD, LCX, RCA) and left ventricle (LV) and right ventricle (RV) layers (subendocardial and subepicardial).

used to define the initial segments of the coronary arteries and the geometric details of the heart wall layers. The coronary arterial tree of the human subject was right dominant, which approximately representing 70% of the general population. Variations of the anatomy of the coronary arterial tree of human are common. The CT dataset consisted of 371 slices of 512×512 transaxial CT images of the entire heart taken at a 0.4 mm slice thickness and a pixel size of 0.32 mm. A total of 100 frames of CT data over one heart cycle were reconstructed. The representative transaxial slices of the CT data at the end-diastolic phase are shown in figure 2.

The main coronary arteries, including the left anterior descending (LAD) artery, the left circumflex (LCX) artery and the right coronary artery (RCA), were manually segmented to define the initial segments. The heart layers, including the subepicardial and subendocardial layers, were also manually segmented to define the geometric boundaries of the myocardium. The 3D NURBS surfaces (Piegl 1991) were fit to the segmented structures of the coronary arteries and heart wall layers, as shown in figure 3. This work was done to assist in the creation of an improved heart model for the XCAT phantom (Segars *et al* 2007).

Table 1. Morphometric statistics of the LAD of the coronary arterial tree.

	Parent vessel order (m)					
	11	10	9	8	7	6
Diameter (μm)	3.176 ± 654	1.492 ± 365	715 ± 130	467 ± 56.1	303 ± 54.5	150 ± 35.8
Length (mm)	2.82 ± 1.96	2.26 ± 1.56	1.54 ± 1.25	1.09 ± 0.83	0.920 ± 0.79	0.609 ± 0.48
Daughter vessel order (n)	Connectivity C(m, n)					
10	0.278	0.010				
9	0.444	0.335	0.017			
8	0.167	0.252	0.352	0.010		
7	0.111	0.201	0.183	0.360	0.023	
6		0.118	0.209	0.272	0.495	
5		0.067	0.192	0.268	0.378	
4		0.017	0.043	0.074	0.075	
3			0.004	0.016	0.024	
2					0.005	

2.1.2. Utilization of coronary arterial tree morphometric data. To extend the segmented tree above, we developed an iterative rule-based generation method based on morphometric data. Statistical details of the coronary arterial tree were essential for generating a realistic coronary arterial tree. The statistical morphometric measurements, including the connectivity matrix, lengths and diameters of each order of the coronary arterial tree, venous network and capillary network, have been thoroughly studied in a number of excised porcine hearts (Kassab *et al* 1993, 1994, 1997, Kassab and Fung 1994). The morphometric data of the coronary arterial tree were used to provide the statistical guidelines for our arterial tree generation. In the animal studies mentioned above, the hearts were excised and prepared with the silicone elastomer-casting method. The measurements were obtained from histological specimens by optical sectioning, or from the vascular cast. According to the findings on porcine hearts, the branching of the arterial tree was dominated by bifurcations, and only a very small number of branches had trifurcation, arcading or anastomose. In our model, the approximation of the branching of the coronary arterial tree is based solely on the bifurcations. The arterial segments were categorized into non-overlapping diameter ranges, from the largest arteries (order 11) to the smallest precapillary arterioles (order 1). The diameters, lengths and connectivity were defined for each vessel order of each main artery. A total of 11 orders of vessels were distributed between the coronary capillaries and the aortic sinus for the RCA and LAD arteries, and 10 orders of vessels were distributed for the LCX artery.

In table 1, the morphometric measurements of the LAD branch of the coronary artery tree are shown as an example. The connectivity, $\mathbf{C}(m, n)$, in the morphometric data was used to calculate the probability of a parent segment of order m having a daughter segment of order n. Thus, the order of one of the two daughter segments at a bifurcation could be stochastically determined based on the connectivity probability distribution. Given the order of the daughter segment, the corresponding diameter and length were chosen from a Gaussian distribution, as defined in table 1. Since the morphometric measurements in Kassab's paper were based on porcine hearts, the diameters and lengths of the vessel segments were required to be linearly
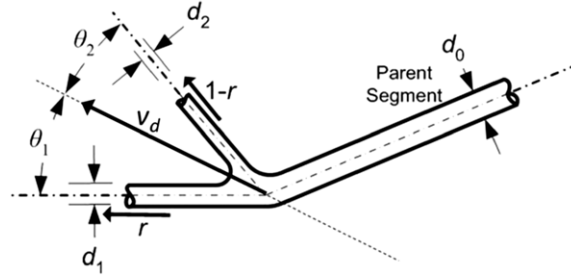
Figure 4. Relationship between flow rate, diameter and branching angle of parent and daughter vessel segments.

scaled to the normal human coronary arteries (Dodge *et al* 1992) before applying them to human coronary arterial tree generation.

2.1.3. Rule-based computer generation of a coronary arterial tree.

Optimal branching angle calculation. The relationship between the diameter of a branch segment and the flow rate through it was first proposed in (Murray 1926) as

$$q = Cd^n, \tag{1}$$

where q is the flow rate, C is a constant that depends on the organ and the fluid, d is the diameter, and n is the diameter exponent, which is a constant. Under the assumption that blood flow obeys Poiseuille's law (Fung 1997), Murray's law (Murray 1926) suggests that for arterial networks with minimized pumping power, the volumetric flow rate in an arterial segment is proportional to the cube of the diameter, i.e. $n = 3$. In a recent study, it was suggested that the flow in human coronary arteries is not entirely steady and laminar (Changizi and Cherniak 2000). Instead of a constant value n, it was argued that values of n should be considered within the range [2,3], $n \in [2, 3]$. In this paper, we obtained the exponent n for each bifurcation by a uniform distributed random number generator with range from 2 to 3.

As shown in figure 4, for a bifurcation site, a parent branch of diameter d_0 has two daughter branches of d_1 and d_2:

$$d_0^n = d_1^n + d_2^n. \tag{2}$$

Using the above relationship, the following equations expressing the diameters of the two daughter branches in terms of the parent diameter and the flow dividing ratio, r, were derived (Kitaoka *et al* 1997):

$$d_1 = d_0 r^{1/n}, \tag{3}$$

$$d_2 = d_0 (1 - r)^{1/n}. \tag{4}$$

The flow dividing ratio is defined as the ratio of the flow rate q_1 through the daughter branch receiving the larger flow rate to the flow rate q_0 of the parent branch, i.e.:

$$r = q_1/q_0, \tag{5}$$

where $0.5 < = r < 1$. The diameter of the daughter branch with the smaller flow rate is less than that with greater flow rate, i.e. $d_1 \geqslant d_2$.

As suggested previously (Hacking *et al* 1996), a drag force or shear stress acting on the lumen walls is the most likely major determinant of branch angle in vascular systems. According to the derivation in (Zamir 1976), the optimal branching angles for minimum shear stress were

$$\theta_1 = \cos^{-1}\left[\frac{\left(q_0^2/d_0^4\right) + \left(q_1^2/d_1^4\right) - \left(q_2^2/d_2^4\right)}{2\left(q_0 q_1/d_0^2 d_1^2\right)}\right],\tag{6}$$

$$\theta_2 = \cos^{-1}\left[\frac{\left(q_0^2/d_0^4\right) + \left(q_2^2/d_2^4\right) - \left(q_1^2/d_1^4\right)}{2\left(q_0 q_1/d_0^2 d_1^2\right)}\right].\tag{7}$$

By substituting equations (3)–(5) into equations (6) and (7), the optimal branching angles are

$$\theta_1 = \cos^{-1}\left[\tfrac{1}{2}\left(r^{\frac{2}{n}-1} + r^{1-\frac{2}{n}} - r^{\frac{2}{n}-1}(1-r)^{2-\frac{4}{n}}\right)\right],\tag{8}$$

$$\theta_2 = \cos^{-1}\left[\tfrac{1}{2}\left(r^{\frac{2}{n}-1} + r^{\frac{2}{n}-1}(1-r)^{2-\frac{4}{n}} - r^{1-\frac{2}{n}}\right)\right].\tag{9}$$

However, the two optimal branching angles were not sufficient for defining the directions of daughter segments in 3D space. The branching plane and the 'combined branching vector', $\mathbf{v_d}$, which will be defined in subsection 2.1.3.4, are required for positioning the daughter segments in 3D space.

Self-avoidance algorithm. To guide the coronary artery tree generation, each existing vessel segment repels the new vascular segment by growing away from its upstream position with a strength inversely related to the distance between the existing and the newly generated vascular segments. The newly generated vasculature tends to grow away from existing structures and toward more sparsely fed layers (Beard and Bassingthwaighte 2000).

As the segments were generated from the largest to the smallest orders, the segments of higher order or previously generated segments of equal order determined the direction of the newly generated segment. As depicted in figure 5, to generate a new segment at bifurcation site $\mathbf{x_c}$, the self-avoidance vector, $\mathbf{v_s}$, was defined as

$$\mathbf{v_s} = \sum \frac{(L/|\mathbf{s_i}|)^\zeta}{1 + (L/|\mathbf{s_i}|)^\zeta}\frac{\mathbf{s_i}}{|\mathbf{s_i}|},\tag{10}$$

where $\mathbf{x_i}$ is the upstream position of all previously generated segments of the same or higher order; $\mathbf{x_c}$ is the upstream position of the current generating segment; $\mathbf{s_i}$ is the vector pointing from $\mathbf{x_i}$ to $\mathbf{x_c}$, i.e. $\mathbf{s_i} = \mathbf{x_c} - \mathbf{x_i}$, as shown in figure 5, $\mathbf{s_p}$ is the one pointing from the immediate parent position; $|\mathbf{s_i}|$ is the absolute distance between $\mathbf{x_i}$ and $\mathbf{x_c}$; ζ is the 'avoidance exponent', governing the degree to which a new segment avoids previously generated segments and $\zeta \approx 2$, and L is the expected length of the current generating segment.

Boundary avoidance algorithm. Another important factor in guiding the coronary artery tree generation is to avoid having arterial segments extend beyond the predefined ventricle wall. The boundaries of the myocardium must constrain the vasculature within the volume defined by the ventricle surfaces, which are the subepicardial and the subendocardial surfaces. As suggested (Beard and Bassingthwaighte 2000), the larger branches (order 9 or larger) should be confined to the subepicardial layer while the smaller branches should be allowed to penetrate into the myocardium.

The myocardial layer is between the subendocardial layer and the subepicardial layer. The NURBS surfaces of the heart, segmented from CT data, were approximated with triangular
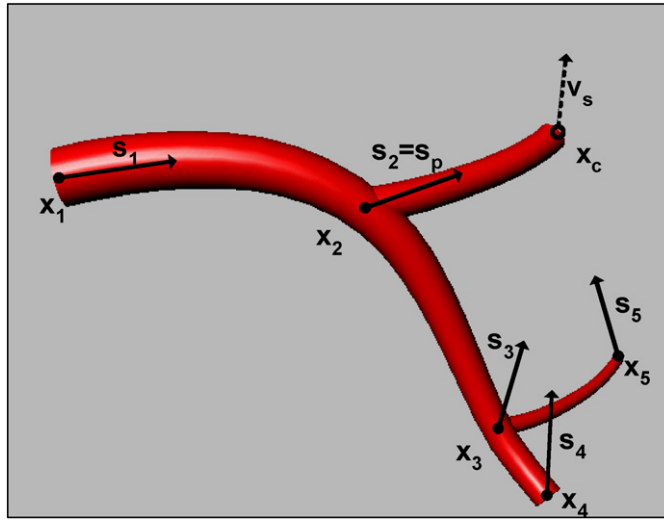
Figure 5. Self-avoidance algorithm.
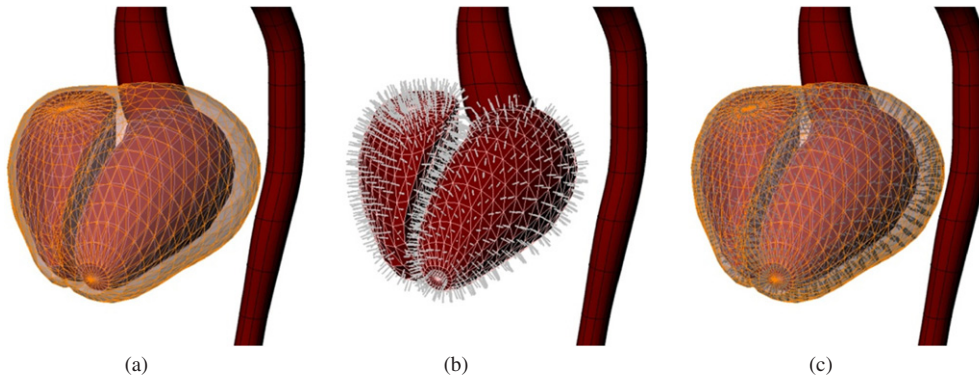
Figure 6. (a) Triangular patch surfaces, (b) subendocardial layer with outward normal vectors and (c) subepicardial layer with inward normal vectors.

surface patches, as shown in figure 6(a). The centroid, area and normal vector were calculated for each triangular patch. The outward pointing normal vectors of the subendocardial layer are depicted in figure 6(b), and the inward pointing normal vectors of the subepicardial layer are depicted in figure 6(c). The larger arterial segments (order 9 and higher) were confined so as to grow along the subepicardial layer. For the smaller arterial segments, they were allowed to penetrate into the myocardial layer due to the combination effect from the self-avoidance from the larger segments in the subepicardial layer and the boundary avoidance from the subepicardial layer. To generate a new daughter segment at bifurcation site $\mathbf{x_c}$, we defined the boundary avoidance vector, $\mathbf{v_b}$, as

$$\mathbf{v_b} = \sum_{j=1}^{N_B} A_j \mathbf{n_j} \, e^{-(|\mathbf{x_c} - \mathbf{c_j}|)/2L}, \tag{11}$$
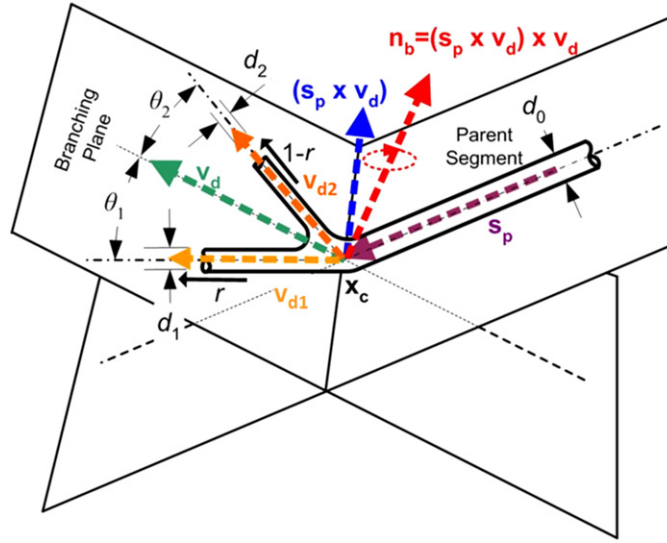
Figure 7. Geometry of defining the branching plane and achieving optimal branching angles.

where N_B is the number of boundary patches within the effective range; A_j is the area of the boundary patch j; $\mathbf{n_j}$ is the (outward or inward) unit normal vector for boundary patch j; $\mathbf{c_j}$ is the centroid of the boundary patch j and L is the expected length of the current generating segment.

Branching plane computation. After calculating the self-avoidance and the boundary avoidance vectors, they were linearly combined to form the 'combined branching vector', $\mathbf{v_d}$, based on empirically determined weighting constants c_s and c_b, defined as

$$\mathbf{v_d} = c_s \frac{\mathbf{v_s}}{|\mathbf{v_s}|} + c_b \frac{\mathbf{v_b}}{|\mathbf{v_b}|}, \tag{12}$$

where $c_s + c_b = 1$.

Since the vessel segment extended into the 3D space, a branching plane was required to confine the direction of the two daughter segments. The normal vector of the branching plane, $\mathbf{n_b}$, was determined by the cross product $\mathbf{s_p} \times \mathbf{v_d}$ with $\mathbf{v_d}$ ($\mathbf{s_p}$ could be slightly perturbed if $\mathbf{s_p}$ is parallel with $\mathbf{v_d}$) as depicted in figure 7 and formulated as

$$\mathbf{n_b} = (\mathbf{s_p} \times \mathbf{v_d}) \times \mathbf{v_d}. \tag{13}$$

Then, $\mathbf{v_d}$ was rotated around the axis $\mathbf{n_b}$ by θ_1 or θ_2 in either a clockwise or counter-clockwise direction to form the daughter branch vectors $\mathbf{v_{d1}}$ and $\mathbf{v_{d2}}$. θ_1 and θ_2 were the optimal branching angles as defined in equations (8) and (9). The directions of the daughter branches were as follows:

for clockwise rotation, $\qquad \mathbf{v_{d1}} = \mathbf{R}_{\theta_1, \mathbf{n_b}} \mathbf{v_d} \quad$ and $\quad \mathbf{v_{d2}} = \mathbf{R}_{-\theta_2, \mathbf{n_b}} \mathbf{v_d};$ $\qquad (14)$

or

for counter$-$clockwise rotation, $\qquad \mathbf{v_{d1}} = \mathbf{R}_{-\theta_1, \mathbf{n_b}} \mathbf{v_d} \quad$ and $\quad \mathbf{v_{d2}} = \mathbf{R}_{\theta_2, \mathbf{n_b}} \mathbf{v_d},$ $\qquad (15)$

where $\mathbf{R}_{\theta_1, \mathbf{n_b}}$ is the rotation matrix which rotates the vector around the axis $\mathbf{n_b}$ by angle θ_1.

The downstream point of the daughter branches was calculated by adding the current bifurcation position to the daughter branch vectors and scaling them by the corresponding nominal lengths L_1 and L_2, which were statistically determined from the morphometric data. They were defined as

$$\mathbf{x_{d1}} = \mathbf{x_c} + L_1 \mathbf{v_{d1}}, \tag{16}$$

and

$$\mathbf{x_{d2}} = \mathbf{x_c} + L_2 \mathbf{v_{d2}}. \tag{17}$$

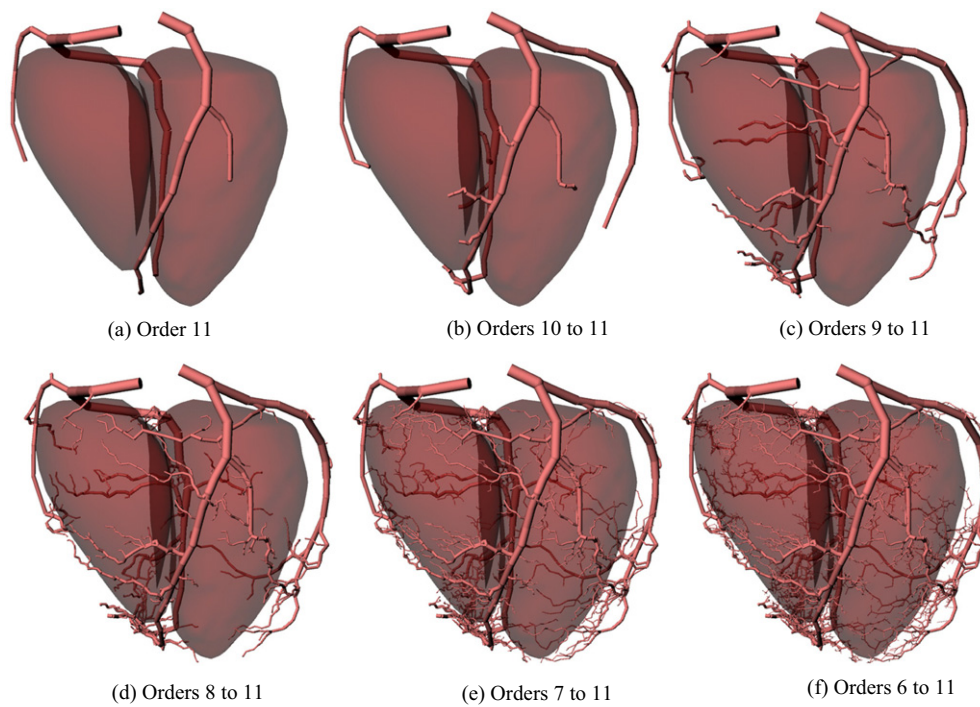Therefore, both $\mathbf{x_{d1}}$ and $\mathbf{x_{d2}}$ were on the branching plane.

Generation rules. Given the morphometry of the coronary arterial tree and fluid dynamic constraint for bifurcations, an iterative generation algorithm, which included self-avoidance and boundary avoidance algorithms, was used to set rules to guide the growth directions of the daughter branches at bifurcations. The rules are summarized as follows:

(1) two daughter branches are produced for each parent branch;
(2) the two daughter branches lie in the branching plane;
(3) the flow rate of the parent branch is conserved after branching;
(4) the diameters of the two daughter branches are statistically determined by the connectivity probability and nominal diameters of the morphometric data under the flow conservation constraint;
(5) the flow-dividing ratio and branching angles are determined by the diameters of the two daughter branches;
(6) the branch length of a given order is determined statistically by the 'scaled' nominal length of the morphometric data;
(7) the larger branches (order 9 or larger) are confined to the subepicardial layer, and the smaller branches are allowed to penetrate into the myocardial layer;
(8) the combined branching vector is determined by the self-avoidance and boundary avoidance algorithms, and
(9) the normal vector of the branching plane is calculated from the parent branch vector and the combined branching vector.

3. Results and discussions

The generation algorithm successively iterated until the segments of the largest six orders of a coronary arterial tree were constructed. The generated coronary arterial tree, including the segments down to orders 11, 10, 9, 8, 7 and 6, with the semi-transparent subendocardial layers of left and right ventricles at the end-diastolic phase, is shown in figures 8(a)–(f), respectively. The six highest order models of the coronary arterial tree that had diameters down to 120 μm, consisted of 2519, 1096 and 2736 segments for the LAD artery, the LCX artery and RCA, respectively.

Figure 9(a) shows a 3D rendering of the highest six orders of the generated coronary arterial tree and the subendocardial layers of the heart defined at end-diastole. By using the cardiac motion vectors of the 4D XCAT phantom defined in our previous publication (Segars *et al* 2009b), the end-diastole model was deformed to end-systole as shown in figure 9(b). The thickened myocardium at the end-systolic phase was clearly reflected as the distance increased between the proximal large arteries and the subendocardial layer, which was prominent at the lateral wall of the left ventricle in figure 9. The longitudinal contraction of the LV toward the apex was largest at the basal region and decreased toward the apical region. The twisting

(a) Order 11

(b) Orders 10 to 11

(c) Orders 9 to 11

(d) Orders 8 to 11

(e) Orders 7 to 11

(f) Orders 6 to 11

Figure 8. Computer-generated coronary arterial tree at different levels of detail and the semi-transparent subendocardial layers of the left and right ventricles at the end-diastolic phase.

(a) End-diastole
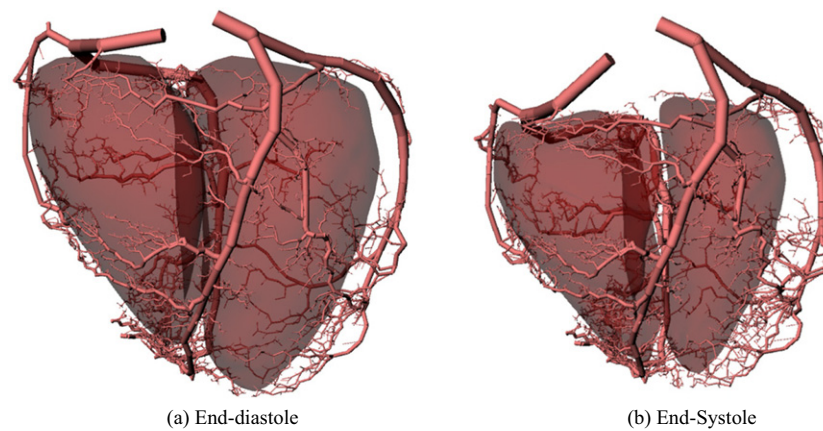
(b) End-Systole

Figure 9. Computer-generated coronary arterial tree at end-diastolic and end-systolic phases with semi-transparent, subendocardial layers of left and right ventricles.

motion could be observed when the image sequence of the generated coronary arterial tree at different phases over a cardiac cycle was displayed.

The level of realism of the generated coronary arterial tree was qualitatively evaluated by two physicians who specialize in cardiac imaging. Their observations were summarized as

follows: (1) the locations and the tracks of the origins, the proximal, middle and distal segments of the LAD, LCX and RCA branches were similar to the typical human heart; (2) the main sub-branches, such as the first and second diagonal, the obtuse marginal, the acute marginal and the posterior descending branches, were located at the typical corresponding regions of the heart; (3) the decreasing diameter of the branches from proximal to distal sub-segments were gradual and consistent; (4) the asymmetric bifurcation pattern of the coronary arterial tree was well matched with the typical human heart, and (5) the proximal large branches were located on the subepicardial layer while the smaller branches penetrated into the myocardium. The physicians also noted a number of potential improvements: (1) the septal branch should penetrate into the septal wall, but not extend over to the right ventricle; (2) some of the distal LAD branches should stay on the left ventricle, and not extend over to the right ventricle, and (3) the arterial segments should be smoothly joined together and not include any sharp turns at the bifurcations. We plan to perform a comprehensive quantitative evaluation study on bifurcation and tapering properties of the coronary arterial tree model, and address the potential improvements in future studies.

4. Conclusion

An anatomically, physiologically and morphometrically realistic 3D model of the coronary arterial tree with cardiac motion was generated by merging knowledge from anatomic CT data, statistical morphometric data of the coronary arterial tree and the cardiac motion of the 4D XCAT phantom. This new model provides an important enhancement to the current 4D XCAT phantom by enabling modeling of a more complete coronary arterial tree in simulation studies for angiography applications. It also has the capability to model MPD for myocardial perfusion SPECT and PET imaging when a perfusion model is applied to the generated coronary arterial tree with a predefined stenosis location (Fung *et al* 2009). The model provides a unique tool for simulating both normal and pathological hearts, which can be used to study and evaluate medical imaging instrumentation and image reconstruction methods for different cardiac imaging modalities.

Acknowledgments

References

Ackerman M J 1999 The visible human project: a resource for education *Acad. Med.* **74** 667–70
Beard D A and Bassingthwaighte J B 2000 The fractal nature of myocardial blood flow emerges from a whole-organ model of arterial network *J. Vasc. Res.* **37** 282–96
Changizi M A and Cherniak C 2000 Modeling the large-scale geometry of human coronary arteries *Can. J. Physiol. Pharmacol.* **78** 603–11
Dodge J T Jr, Brown B G, Bolson E L and Dodge H T 1992 Lumen diameter of normal human coronary arteries *Circulation* **86** 232–46
Fung G S K, Segars W P, Veress A I, Gullberg G T and Tsui B M W 2009 Toward modeling of regional myocardial ischemia and infarction: Generation of realistic coronary arterial tree for the heart model of the XCAT phantom *Proc. SPIE* **7262** 1–6
Fung Y C 1997 *Biomechanics: Circulation* 2nd edn (New York: Springer) pp 10–12 chapter 1
Garrity J M, Segars W P, Knisley S B and Tsui B M W 2003 Development of a dynamic model for the lung lobes and airway tree in the NCAT phantom *IEEE. Trans. Nucl. Sci.* **50** 378–83

Hacking W J, VanBavel E and Spaan J A 1996 Shear stress is not sufficient to control growth of vascular networks: a model study *Am. J. Physiol.* **270** H364–75

Kaimovitz B, Lanir Y and Kassab G S 2005 Large-scale 3D geometric reconstruction of the porcine coronary arterial vasculature based on detailed anatomical data *Ann. Biomed. Eng.* **33** 1517–35

Kaimovitz B, Lanir Y and Kassab G S 2010 A full 3D reconstruction of the entire porcine coronary vasculature *Am. J. Physiol. Heart. Circ. Physiol.* **299** H1064–76

Kassab G S, Berkley J and Fung Y C 1997 Analysis of pig's coronary arterial blood flow and detailed anatomical data *Ann. Biomed. Eng.* **25** 204–17

Kassab G S and Fung Y C 1994 Topology and dimensions of pig coronary capillary network *Am. J. Physiol.* **267** H319–25

Kassab G S, Lin D H and Fung Y C 1994 Morphometry of pig coronary venous network *Am. J. Physiol.* **267** H2100–13

Kassab G S, Rider C A, Tang N J and Fung Y C B 1993 Morphometry of pig coronary arterial tree *Am. J. Physiol.* **265** H350–65

Kitaoka H, Takaki R and Suki B 1997 A three-dimensional model of the human airway tree *J. Appl. Physiol.* **82** 968–76

McGurk R *et al* 2010 Extension of the NCAT phantom for the investigation of intra-fraction respiratory motion in IMRT using 4D Monte Carlo *Phys. Med. Biol.* **55** 1475–90

Minarik D, Ljungberg M, Segars P and Gleisner K S 2009 Evaluation of quantitative planar 90Y bremsstrahlung whole-body imaging *Phys. Med. Biol.* **54** 5873–83

Murray C D 1926 The physiological principle of minimum work *Proc. Natl Acad. Sci.* **12** 207–14

Piegl L 1991 On NURBS: a survey *IEEE Comput. Graph. Appl.* **11** 55–71

Segars W P 2001 Development and application of the new dynamic NURBS-based cardiac-torso (NCAT) phantom *PhD Thesis* Biomedical Engineering, University of North Carolina

Segars W P, Lalush D S, Frey E C, Manocha D, King M A and Tsui B M W 2009b Improved dynamic cardiac phantom based on 4D NURBS and tagged MRI *IEEE Trans. Nucl. Sci.* **56** 2728–38

Segars W P, Mahesh M, Beck T J, Frey E C and Tsui B M W 2008 Realistic CT simulation using the 4D XCAT phantom *Med. Phys.* **35** 3800–8

Segars W P, Mendonca A, Sturgeon G and Tsui B M W 2007 Enhanced 4D heart model based on high resolution dual source gated cardiac CT images *IEEE Medical Imaging Conf. Record* pp M04–1

Segars W P, Mok S P and Tsui B M W 2009a Investigation of respiratory gating in quantitative myocardial SPECT *IEEE Trans. Nucl. Sci.* **56** 91–6

Segars W P, Sturgeon G, Mendonca S, Grimes J and Tsui B M W 2010 4D XCAT phantom for multimodality imaging research *Med. Phys.* **37** 4902–15

Segars W P and Tsui B M W 2009 MCAT to XCAT: the evolution of 4D computerized phantoms for imaging research *Proc. IEEE* **87** 1954–68

Segars W P, Tsui B M W, Frey E C and Fishman E K 2003 Extension of the 4D NCAT phantom to dynamic x-ray CT simulation *IEEE Medical Imaging Conf. Record* pp 3195–9

Smith N P, Pullan A J and Hunter P J 2000 Generation of an anatomically based geometric coronary model *Ann. Biomed. Eng.* **28** 14–25

Tang J, Rahmin A, Lautamaki R, Lodge M A, Bengel F M and Tsui B M W 2009 Optimization of Rb-82 PET acquisition and reconstruction protocols for myocardial perfusion defect detection *Phys. Med. Biol.* **54** 3161–71

Zamir M 1976 Optimality principles in arterial branching *J. Theor. Biol.* **62** 227–51